Nanotexturing TiO2 over carbon nanotubes for high-energy and high-power density pseudocapacitors in organic electrolytes

N. Poirot, V. Rajalingam, R. Murgu, R. Omnée, E. Raymundo-Piñero

To cite this version:

N. Poirot, V. Rajalingam, R. Murgu, R. Omnée, E. Raymundo-Piñero. Nanotexturing TiO2 over carbon nanotubes for high-energy and high-power density pseudocapacitors in organic electrolytes. Frontiers in Materials, 2022, 9, pp.1011782. ⟨10.3389/fmats.2022.1011782⟩. ⟨hal-03852535⟩

HAL Id: hal-03852535

https://hal.science/hal-03852535v1

Submitted on 23 Nov 2022

Frontiers in Materials

TYPE Original Research
PUBLISHED 07 October 2022
DOI 10.3389/fmats.2022.1011782

OPEN ACCESS

EDITED BY
Muhammad N. Huda,
University of Texas at Arlington,
United States

REVIEWED BY
Zhengpeng Yang,
Henan Polytechnic University, China
Biplab Kumar Kuila,
Banaras Hindu University, India

*CORRESPONDENCE
E. Raymundo-Piñero,
raymundo@cnrs-orleans.fr

SPECIALTY SECTION
This article was submitted to Carbon-Based Materials,
a section of the journal
Frontiers in Materials

RECEIVED 04 August 2022
ACCEPTED 26 September 2022
PUBLISHED 07 October 2022

CITATION
Poirot N, Rajalingam V, Murgu RN, Omnée R and Raymundo-Piñero E (2022), Nanotexturing TiO_2 over carbon nanotubes for high-energy and high-power density pseudocapacitors in organic electrolytes.
Front. Mater. 9:1011782.
doi: 10.3389/fmats.2022.1011782

Nanotexturing TiO_2 over carbon nanotubes for high-energy and high-power density pseudocapacitors in organic electrolytes

N. Poirot[1], V. Rajalingam[1,2], R. N. Murgu[1,2], R. Omnée[2,3] and E. Raymundo-Piñero[2,3]*

[1]GREMAN, François Rabelais University, Blois, France, [2]CNRS, CEMHTI UPR 3079, Univ. Orléans, F - 45071 Orléans, France, [3]Réseau sur le Stockage Électrochimique de L'Énergie (RS2E), FR CNRS 3459, Amiens, France

Titanium oxides have been considered potential electrode materials for pseudocapacitors because of their exceptional properties, such as high thermal and chemical stabilities, ready availability and low cost. However, they are not ideal for practical applications due to their poor ionic and electrical conductivity. The electrochemical performance of TiO_2 can be greatly improved if the material is nanotextured by reducing the particle size in optimizing the synthesis pathway. Actually, for metallic oxides, the electrochemical performance significantly depends on the particle size/morphology. At relatively low current densities the higher capacity values are exhibited by noncrystalline TiO_2 having 2 nm particle size, with values reaching 704 C g^{-1}. However, only thin electrodes are able to operate at a high charge density, limiting the energy density of the final device. Here, we propose a solution to circumvent such a drawback by further nanotexturing TiO_2 over multiwalled carbon nanotubes (CNTs). For that purpose, CNTs were introduced during oxide preparation. The synthesis protocol has been optimized for obtaining a uniform coverage of small TiO_2 particles on the surface of the CNTs. At low current densities, high mass loading TiO_2/CNT composites electrodes are able to deliver capacitances as high as 480 F g^{-1} and the presence of CNTs allows keeping 70% of the capacitance at high current densities while only 27% is retained when using a regular conductivity agent as carbon black. The results demonstrate that uniform nanotexturation of TiO_2 over CNTs allows good rate capabilities to be obtained for thick electrodes having sufficient active material loading to achieve high specific energy and power densities.

KEYWORDS

nanotexturation, pseudocapacitor, TiO_2, organic electrolyte, thick electrodes

Introduction

For decades, the study of metal oxides as electrodes for supercapacitors has exponentially grown to find alternative materials to commonly used porous carbon (Augustyn et al., 2014; Choudhary et al., 2017; Razaa et al., 2018; Lokhande et al., 2019). Developing nanomaterials and nanostructured materials is a key issue for obtaining materials with good electrochemical performances (energy density, power density and cycle life) in the field of energy storage devices (Zheng and Jow, 1995; Devaraj and Munichandraiah, 2008; Ghodbane et al., 2009; Hu et al., 2009; Chen et al., 2010; Augustyn et al., 2014; Choudhary et al., 2017; Razaa et al., 2018; Lokhande et al., 2019). With such materials, some effect resembling capacitance can arise when the transfer of a faradaic charge is proportional or approximately proportional to the applied voltage. This kind of capacitance, of faradaic and not electrostatic origin, is distinguished from the double-layer capacitance and called “pseudocapacitance”. The mechanism of the pseudofaradic reactions at the origin of the capacitance depends on the nature of the electrolyte. In aqueous electrolytes, this mechanism can be simply expressed by a redox reaction that is common to most transition metallic oxides (Chen et al., 2010):

$$MO_2 + X^+ + e^- \leftrightarrow MOOX \tag{1}$$

where M is the transition metal and X represents hydrated protons (H_3O^+) and/or alkali cations from the electrolyte such as K^+, Na^+ and Li^+. The most interesting materials are RuO_2 and MnO_2 because several redox processes overlap over a wide potential range (Zheng and Jow, 1995; Devaraj and Munichandraiah, 2008; Ghodbane et al., 2009; Chen et al., 2010; Augustyn et al., 2014; Choudhary et al., 2017; Razaa et al., 2018; Lokhande et al., 2019). For other materials, such as oxyhydroxides of Co or Ni, capacitive behavior arises due to a single redox process involving electron injection/removal; therefore, the effective operating voltage is very low (Zheng and Jow, 1995; Zhao et al., 2007; Hu et al., 2009; Augustyn et al., 2014). Other metallic oxides, such as Fe_3O_4 (Chen et al., 2014), Bi_2O_3 (Xu et al., 2015), TiO_2 (Zhou and Zhang, 2014), SnO_2 (Zhou and Zhang, 2014), CuO_2 (Xu et al., 2016), V_2O_5 (Zhang et al., 2016), NiOx (Gao et al., 2013), MoO_3 (Barzegar et al., 2015) and Co_3O_4 (Liu et al., 2018), have been studied in research on environmentally friendly and pseudocapacitive compounds with electrochemical performances similar to those of RuO_2 or even MnO_2 in aqueous electrolytes. However, the main drawback for metallic oxides is that their ionic and electronic conductivity is generally low, and to maximize the rate capability, it is necessary to use thin films that minimize the amount of energy stored.

In organic electrolytes, Li intercalation into host materials, such as TiO_2, MnO_2, and CeO_2, used for Li-ion batteries can be regarded in some sense as pseudocapacitance since the charge exchanged could be an almost continuous function of potential (Brousse et al., 2015; Huang et al., 2015). Although their response time is longer than that for double layer charging owing to the necessity for interlayer diffusion in the solid host lattice, Li^+ ion accommodation is reported as a quasi-2-dimensional phenomenon occurring on the material layer surfaces, similar to the adsorption pseudocapacitance observed in aqueous electrolytes.

As an example, MnO_2 can also demonstrate capacitive behavior in organic electrolytes when using a Li-based salt due to Li insertion/disinsertion (Jiao and Bruce, 2007) according to Equation 1:

$$MnO_2 + \delta Li^+ + \delta e^- \leftrightarrow Li_\delta MnO_2 \tag{2}$$

However, an enhanced electronic conductivity and a large degree of active surface accessibility are mandatory for obtaining capacitance values as high as those in aqueous electrolytes (Brandt and Balducci, 2014). The advantage in organic electrolytes is that the stability potential window (from 1.5 to 3.5 V vs. Li/Li^+) is larger than the 0.8–1.0 V window in aqueous solution and the consequently higher extractable energy. Nevertheless, for such materials, strategies such as nanotexturation should be introduced to achieve charge capacities comparable to those found in batteries without compromising high charging/discharging rates (Wang et al., 2007; Brezesinski et al., 2009). Actually, this was first reported for anatase TiO_2 nanocrystals, where pseudocapacitive effects related to the charge storage of Li^+ cations from faradic processes occurring on the surface, similar to the adsorption capacitance, became increasingly important when the electroactive material approached nanoscale dimensions. The pseudocapacitive contribution to faradic processes increases with decreasing the particle size down to 10 nm; i.e., the potential-dependent contribution increases from 15 to 55% when the particle size decreases from 30 to 7 nm. This pseudocapacitive contribution leads to higher levels of total stored charge than in the corresponding bulk material and much faster charge/discharge kinetics (Wang et al., 2007).

For these reasons, the direction taken by several studies consists of synthesizing crystalline porous nanostructures with large surface areas to ensure that the surface, not the bulk, dominates the electrochemical properties. In this sense, nanostructured TiO_2 has been reported for energy storage applications in the form of nanoparticles, fibers, nanotubes, nanocages, nanorods, nanowires and nanoribbons (Wang et al., 2006 and, Wang et al., 2016; Salari et al., 2011; Shao et al., 2015; Wang et al., 2007; Szeifert et al., 2010; Gao et al., 2020; Chen and Mao, 2007; Wang and Lou, 2012; Yu et al., 2017; Ramandoss and Kim, 2013; Ge et al., 2016; Lu et al., 2013). Unfortunately, all these reports based on titanium oxide electrodes lack a systematic study of the particle size effect. Moreover, the synthesis routes proposed for producing such nanotextured materials are quite complicated and/or require hazardous chemicals. As an example, nanotubular and nanoporous modified structures of TiO_2 are prepared by anodization of titanium in hydrofluoric acid (HF)-containing electrolytes (Mor et al., 2005), or mesoporous titania can be produced by using a template in the presence of surfactants (Chen et al., 2009). Hence, the use of environmentally unfriendly and unsafe chemicals such as HF and surfactants may limit interest in such synthesis techniques.

Among the mildest synthesis pathways in the solution phase, the sol–gel method is one of the most common and low-cost methods that is able to produce metal oxide nanoparticles with fine control of the particle size, morphology, pore size and surface area (Courtin et al., 2012; Chen and Kumar, 2012; Poirot et al., 2015; Cargnello et al., 2014; Subramanian et al., 2006; Sudant et al., 2005; Jiang et al., 2007; Debecker and Mutin, 2012; Cushing et al., 2004; Niederberger and Garnweitner, 2006, Niederberger, 2007 and Niederberger et al., 2002). The sol–gel method allows the control of the morphology, porosity, size and distribution of particles. By exploiting the nature of the precursors and solvents, their concentration ratios and the different synthesis parameters, nanostructured materials with controlled morphology can be obtained. The sol–gel chemistry allows the preparation of homogeneous solutions containing either nanoparticles (colloidal sol) or molecular species (polymeric sol), leading to porous or dense nanostructured materials. Sol–gel chemistry has many advantages in processing TiO_2 nanoparticles, such as good control of solution homogeneity, small size and low processing temperatures (Sudant et al., 2005; Subramanian et al., 2006). An interesting way to synthesize TiO_2 nanoparticles is the use of nonaqueous sol–gel processes in organic solvents. The use of organic solvents to drive nonhydrolytic condensation reactions overcomes some of the major limitations of aqueous systems, as they act as oxygen-supplying agents for metal oxides and strongly influence particle size, shape and crystallinity at low temperatures (Debecker and Mutin, 2012; Cushing et al., 2004; Niederberger and Garnweitner, 2006, Niederberger, 2007 and Niederberger et al., 2002). Moreover, nonaqueous sol–gel processes have been shown to be efficient for developing hybrid materials with ultradispersed anatase TiO_2 nanoparticles on graphene exhibiting good electrochemical performance in energy storage devices (Li et al., 2013).

In this work, we present a sol–gel method without using any surfactants or additives to prepare TiO_2 nanoparticles with particle sizes less than 5 nm in the anatase phase, which is generally considered to be a more electroactive lithium-ion insertion host than other TiO_2 polymorphs (Wang et al., 2007). The electrochemical behavior of the materials used as electrodes for supercapacitors was characterized in an organic electrolyte containing a Li salt. The electrochemical performance of TiO_2 can be greatly improved if the material is nanotextured by reducing the particle size in optimizing the synthesis pathway. However, only thin electrodes are able to operate at high charge density, limiting the energy density of the final device. Here, we propose a solution to circumvent such a drawback by further nanotexturing TiO_2 over multiwalled carbon nanotubes (CNTs). For this purpose, CNTs were introduced during oxide preparation. The synthesis protocol was optimized to obtain uniform coverage of small TiO_2 particles on the surface of the CNTs. The results show that the TiO_2/CNT composites allow thick electrodes to have high capacitance and the rate capability desired for developing supercapacitors with high energy density and high power density.

Materials and methods

Synthesis of TiO_2 nanoparticles

Anatase TiO_2 nanoparticles were prepared by the sol–gel route using tetrabutyl titanate (TBT, Acros Organics, 99%) as a titanium oxide precursor. In a typical procedure, 3 ml of TBT was added dropwise to 30 ml of ethanol. The clear solution was mixed with vigorous constant magnetic stirring at room temperature (RT) for 10 min. After that, 30 ml of deionized water was added slowly to the solution, allowing TiO_2 formation. The final solution concentration was close to 0.14 $mol\ L^{-1}$. The mixture (white color suspension) was then transferred into a round bottom flask and refluxed for 4 h at 65°C. TiO_2 powder was collected after centrifugation, washed with ethanol and deionized water repeatedly, and dried at 100°C or 120°C overnight. The samples are denoted 4hR_100 and 4hR_120 (R stands for reflux, 4 h for the time of reflux and 100 or 120 for the temperature of drying). For comparison, TiO_2 powders were also produced at RT by simple magnetic stirring of the TBT–ethanol–water mixture for 0.25 h without refluxing and dried overnight at 100°C and 120°C. The samples are denoted 0.25hM_100 and 0.25hM_120 (M stands for magnetic stirring, 0.25 h for the time of stirring and 100 or 120 for the temperature of drying).

Synthesis of TiO_2/CNT composites

TiO_2/CNT composites were further obtained by the same methods: stirring and reflux synthesis. Physicochemical characterization of the CNTs (CCVD, Groupement de Recherches de Lacq, Arkema, France) can be found elsewhere (Raymundo-Piñero et al., 2005; Raymundo-Piñero et al., 2011). In two routes, suitable amounts of TBT and CNTs were dispersed in mixed solvents of ethanol and water (1:1 in volume) to obtain composites with 10 wt% and 20 wt% CNTs. Part of the solution was sampled after 0.25 h of mixing, and the other part was refluxed for 4 h at 65°C. Another synthesis route consists of ultrasonically dispersing the same initial solution for 2 h. Irradiation was carried out with an interval of 5 s every 30 s. Then, the solution was refluxed for 2 additional hours. For all synthesis routes, the formed milky suspension was collected by centrifugation. The unreacted reagents were removed by washing the precipitate with ethanol and DIW three times and dried at 100°C overnight in air. The composites obtained by mixing were named 0.25hM10 and 0.25hM20 since the ones obtained by reflux are named 4hR10 and 4hR20 and the ones obtained by sonication and reflux are 4hSR10 and 4hSR20 (here S stands for sonication). The 10 and 20 at the end of the names represent 10 wt% CNTs and 20 wt% CNTs, respectively.

Physicochemical characterization

X-ray diffraction (XRD) analysis was conducted on a Bruker D8 Advance diffractometer equipped with Cu Kα radiation (λ = 0.15418 nm, 40 kV and 40 mA). The XRD powder patterns were collected from 20 to 80° with a 2θ step size of 0.02°. The crystallite size was determined by the Debye–Scherrer formula. Field-emission scanning electron microscopy (FE-SEM) images were recorded using a Carl Zeiss Ultra 55 system to examine the morphology and microstructure of the as-obtained samples. Transmission electron microscopy (TEM) images and selected area electron diffraction (SAED) patterns were taken by a JEOL-JEM-2100 system at an accelerating voltage of 200 kV.

Nitrogen adsorption isotherms were recorded at 77 K using a Quadrasorb (Quantachrome, USA) instrument for relative pressure (P/P_0) values between 10^{-5} and 1. The samples were preliminarily outgassed for 12 h at 120°C. The Brunauer–Emmett–Teller equation was applied to calculate the specific surface area (S_{BET}), and the pore size distribution was determined using the nonlinear density functional theory approach (NLDFT).

Electrochemical characterization

Electrodes were prepared by mixing TiO_2 (70 wt%) with a conductive additive (20 wt%,carbonblack (Pureblack®, Superior Graphite Co.)) and a binder (10 wt%, polyvinylidene fluoride) in ethanol. The resulting paste was rolled up to obtain a self-standing film, and 1 cm-diameter electrodes were punched. Composite TiO_2-CNT electrodes were prepared by mixing the active material (90 wt%) with the binder (10 wt%) by following the same procedure used to obtain the self-standing films. Labels as “thin” and “thick” has been added to indicate the electrode mass loading. The label “thin” after the sample name indicates an electrode mass loading of approximately 1.5 mg cm^{-2} since “thick” refers to electrodes with a mass loading of approximately 9.0 mg cm^{-2}.

Three-electrode Swagelok® cells were assembled in a glove box (filled with high-purity argon) with the TiO_2 material as the working electrode and lithium metal as the counter and reference electrodes using 1 mol L^{-1} $LiPF_6$ in EC/PC/3DMC as the electrolyte. Electrochemical characterization of the materials was carried out with cyclic voltammetry (1 mV s^{-1}) and galvanostatic charge/discharge cycling (0.1–3 A g^{-1}) in a potential window from 1 to 3.5 V vs. Li/Li$^+$ with a VMP3 multichannel potentiostat/galvanostat (Bio-Logic, France).

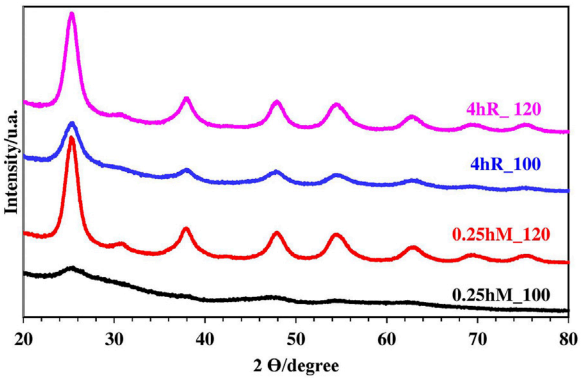

FIGURE 1
XRD patterns of TiO_2 materials.

Results and discussion

Physicochemical characterization TiO_2

XRD patterns are shown in Figure 1. The figure shows that all samples are well crystallized in anatase TiO_2 (space group: $I4_1/amd$, JCPDS N°. 21–1,272), except for the 0.25hM_100 sample, which is amorphous. An additional diffraction peak is observed at 30.8°, indicating the presence of a minor brookite phase ((121) peak, JCPDS N°. 29–1,360). It is well known that the anatase phase is the main product in hydrolytic sol–gel synthesis, with the brookite phase often presenting as a minor secondary product. According to the literature (Zhang and Banfield, 2000), the ratio between the two phases can be obtained by calculating the ratio between the intensities of the anatase (101) diffraction peak and the brookite 121) peak. For all materials, less than 1% of the brookite phase is obtained. The average particle sizes of the different TiO_2 materials, determined from Scherrer’s formula taking the (101) peak as a reference, are shown in Table 1. The table shows that the particle size is always smaller than 5 nm and that an average size as small as 3.7 nm can be obtained when TiO_2 synthesis is done under reflux conditions and the drying temperatures does not exceed 100°C.

Figure 2 illustrates the surface morphology of TiO_2 materials obtained using different synthesis conditions determined by FE-SEM. The morphology depends on the synthesis method, in particular, the agglomeration. Figure 2A shows that stirring the

TABLE 1 TiO_2 materials prepared with different experimental conditions. Particle size, specific surface area and capacity obtained in a $LiPF_6$ EC/PC/3DMC electrolyte at a current of 0.1 A g^{-1}.

Sample	Particle size nm	Surface area m^2/g	Capacity C/g_{TiO2}	Capacity mAh/g_{TiO2}
0.25hM_100	2.0[a]	486	704	196
0.25hM_120	4.8	296	644	179
4hR_100	3.7	400	448	124
4hR_120	5.1	302	581	161

[a]Estimated from TEM.

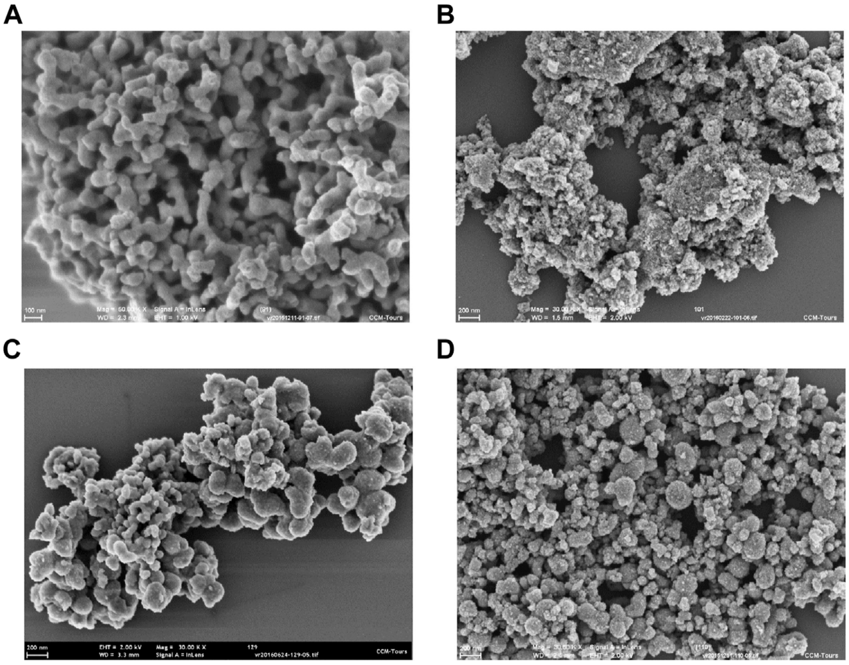

FIGURE 2
SEM images of TiO_2 nanomaterials: **(A)** 0.25hM_100, **(B)** 0.25hM_120, **(C)** 4hR_100 and **(D)** 4hR_120.

solution of the TiO_2 precursor for just 15 min and performing gentle drying at a temperature close to the solvent boiling point (i.e., boiling point of 81°C, drying temperature of 100°C) drives the agglomeration of TiO_2 particles in a branched morphology (sample 0.25hM). The TiO_2 nanoparticles aggregate into entangled branches with a length/diameter ratio greater than 3.5, average diameters close to 50 nm and lengths up to 500 nm. Figure 2B shows the morphology of TiO_2 after following the same synthesis pathway but performing the drying step at a slightly higher temperature; i.e., 120°C is completely different. Drying at a temperature higher than the solvent boiling point induces faster particle deposition, and they do not have time to arrange into branches. Instead, they aggregate into particles with an irregular morphology with great particle size dispersion. Figures 2C,D show that including a 4-h refluxing step of the TiO_2 precursor–solvent mixture in the synthesis protocol led to a different morphology (sample 4hR). Figure 2C illustrates that if the mixture is gently dried at 100°C, TiO_2 nanoparticles aggregate into ellipsoidal morphologies with diameters ranging from 50 nm to 300 nm (sample 4hR_100). If the refluxed mixture is dried faster at a higher temperature (sample 4hR_120), Figure 2D shows how the ellipsoidal–spheroidal aggregates become more isolated.

According to the TEM images, TiO_2 nanoparticles are pseudospherical in shape with a more or less uniform size distribution. The TEM image in Figure 3A shows that the particle size obtained by simply stirring the TBT–solvent mixture and drying at low temperature (0.25hM_100 sample) is very small. The average diameters range between 1 and 2 nm. The nanoparticles are densely self-

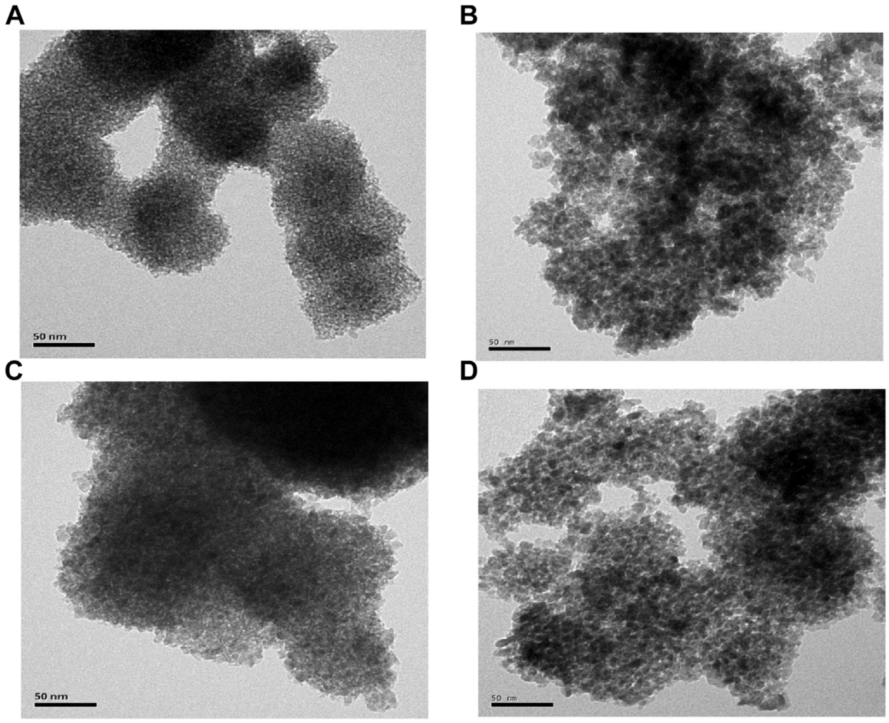

FIGURE 3
TEM images of TiO_2 nanomaterials: **(A)** 0.25hM_100, **(B)** 0.25hM_120, **(C)** 4hR_100 and **(D)** 4hR_120.

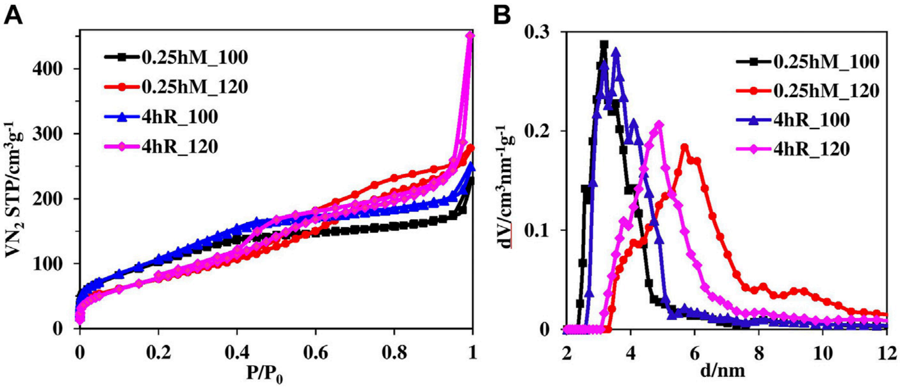

FIGURE 4
Porous texture characterization of TiO_2 materials: **(A)** N_2 gas adsorption isotherms and **(B)** DFT pore size distribution.

assembled into aggregates with the branched morphology previously observed by SEM. When increasing the drying temperature (sample 0.25hM_120, Figure 3B), the TiO_2 particles are larger in size, with diameters ranging between 4 and 5 nm, and they are less densely packed. Adding the solution in the reflux step during synthesis (sample 4hR_100 in Figure 3C) also results in a larger particle size, with diameters ranging between 3 and 4 nm. The drying temperature seems to have the same effect as that for the materials prepared without refluxing, as the particles are slightly larger upon increasing the temperature from 100°C to 120°C (samples 4hR_100 and 4hR_120 in Figures 3C,D,

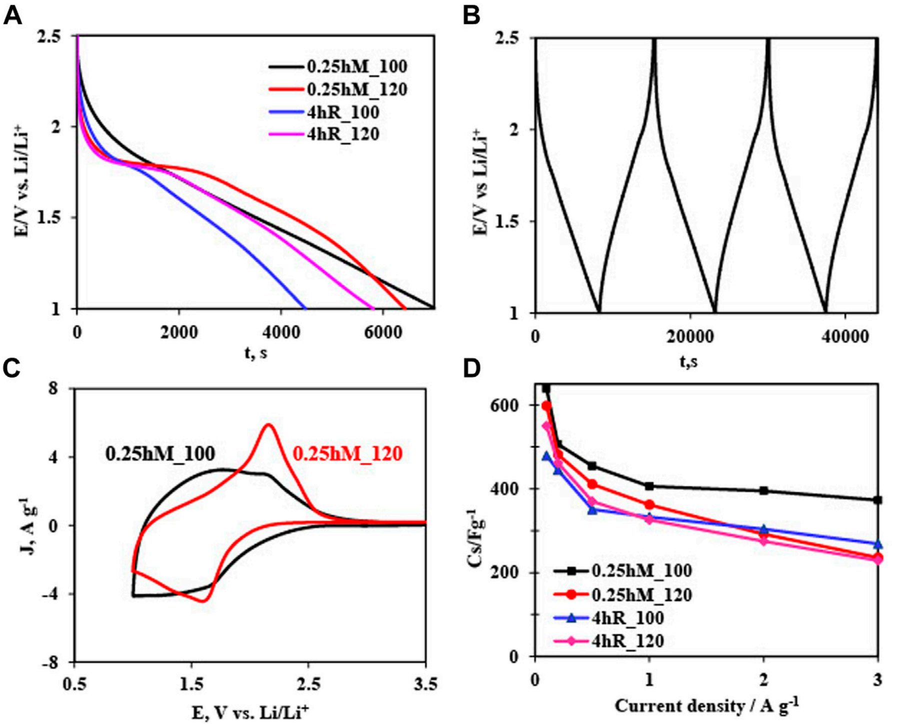

FIGURE 5
Electrochemical characterization of TiO_2 materials using $LiPF_6$ EC/PC/3DMC electrolyte: **(A)** galvanostatic discharge profile at a charge density of 0.1 A g^{-1}, **(B)** galvanostatic charge–discharge profile on 0.25hM_100 TiO_2 at a charge density of 0.1 A g^{-1}, **(C)** Cyclic voltammetry at 2 mV s^{-1} on 0.25hM_100 and 0.25hM_120 TiO_2 and **(D)** comparison of rate capabilities.

respectively), and the particle packing density is clearly higher for the material treated at lower temperatures.

Figure 4 shows the N_2 adsorption isotherms and the pore size distributions (PSDs) for the different materials. The isotherms of all the materials present hysteresis loops at high relative pressures, which is typical for a mesoporous material. TiO_2 0.25h_100 presents a surface area as large as 486 m^2 g^{-1} with small mesopores with diameters ranging from 2 to 4 nm. Such results are in concordance with the morphology of the sample with small TiO_2 nanoparticles (approximately 2 nm, see the TEM image in Figure 3) aggregated into high-density branches. When synthesis is performed under reflux conditions using longer mixture times, i.e., 4 h, the particle size is still small (3.7 nm), but particle agglomeration drives the presence of the largest amount of small mesopores with a diameter of approximately 2–5 nm. However, the specific surface area reaches a similar large value of 400 m^2 g^{-1}. As mentioned above, the drying temperature has a great impact on the particle size and agglomeration. When increasing the drying temperature from 100°C to 120°C, TiO_2 particles tend to agglomerate into spheroidal particles (see the TEM image in Figure 3), leading to less dense material with a wider mesopore size distribution ranging from 3 to 8 nm in diameter, as shown in Figure 4. As a result, the specific surface area of the materials dried at 120 °C is smaller than that of the materials dried at 100°C (see Table 1), remaining at approximately 300 m^2 g^{-1}.

In conclusion, crystallinity, particle size, agglomeration density and morphology depend on the synthesis conditions. Such parameters have a clear impact on the specific surface area, and the pore size distribution is crucial for the electrode/electrolyte interface and electrochemical performance.

Electrochemical characterization of TiO_2

Electrodes of the materials synthesized above were prepared by using 20 wt% carbon black as a conductive agent. The electrochemical characterization of the different materials was first performed by galvanostatic charge/discharge at a very low charge density of 0.1 A g^{-1}, which corresponds to approximately C/2. Such small charge densities allow discrimination of redox reactions, i.e., faradic reactions, from pseudofaradic reactions. Three different regions are generally observed for TiO_2 in the galvanostatic discharge curve (Figure 5A). The first sloped region at high potentials has been previously related either to the formation of a solid solution of anatase and lithiated anatase

(Sudant et al., 2005) or a capacitive-like surface process at the electrode/electrolyte interface (Jiang et al., 2007). The second region presenting a potential plateau corresponds to the Faradic process of Li insertion into the octahedral sites of the anatase crystals. The sloped region at low potentials has been related to further insertion of Li ions into the surface TiO_2 layer. Figure 5A shows that as expected (Sudant et al., 2005; Jiang et al., 2007; Wang et al., 2007), the electrochemical signature during the charging/discharging of oxides such as TiO_2 is strongly affected by the particle size. In particular, the faradic contribution decreases when decreasing the particle size as diffusion-controlled lithium-ion intercalation processes are replaced by surface reactions (Wang et al., 2007). The figure shows that for the materials with an amorphous nature having a small particle size of approximately 2 nm, such as 0.25hM_100, the electrochemical signature is purely capacitive, with a constant variation of potential with time. However, for the material with higher crystallinity and a slightly larger particle size of 3.7 nm (4hR_100), a very small faradic contribution at 1.8 V vs. Li/Li^+ during discharge is detected in the galvanostatic profile. Finally, for the materials with larger particle sizes of approximately 5 nm (0.25hM_120 and 4hR_120), the faradic contributions related to the insertion of Li ions at the anatase crystal lattice are more visible in the galvanostatic profile.

Therefore, the discharge profile depends on the physicochemical properties of the TiO_2 material. For the first discharge step at higher potentials, the capacity follows the same trend as the specific surface area of the materials, indicating that the charging mechanism is surface related. In particular, the material with the narrower pore size distribution having average pore sizes in the range of small mesopores (0.25hM_100) driving to higher specific surface areas presents a much higher capacity. The second region in the discharge curves most likely depends on the particle sizes and crystallinity. In addition to the fact that there is not a plateau for the amorphous material, for materials with the anatase structure, the extension of the plateau depends on the particle size, with an almost negligible plateau for the anatase material with the smaller particle size, i.e., 3.7 nm, indicating the minor presence of octahedral sites for Li insertion. For the third region, at potentials lower than 1.7–1.8 V vs. Li/Li^+, there is not a unique slope for the crystalline materials, indicating that different energy levels are accessible for Li insertion into the surface layer because of the small particle size (Razaa et al., 2018). In contrast, for the amorphous material, there is a unique slope with a linear decrease in potential vs. time because decreasing the particle size to values smaller than 2–3 nm broadens the energy levels accessible in the materials, and the amorphous nature favors the surface process. Finally, the amorphous material with a small particle size and a large surface area with a narrow pore size distribution behaves as a capacitive material, even at low current densities with a triangular charge/discharge curve (Figure 5B). The differences in charge mechanism with the particle size are also visible when performing cyclic voltammetry as presented in Figure 5C. The redox peak related to Li ion insertion in the 0.25hM_120 material with larger particle size is clearly visible while the 0.25hM_100 material having smaller particle size presents a capacitive like behavior without visible redox peaks.

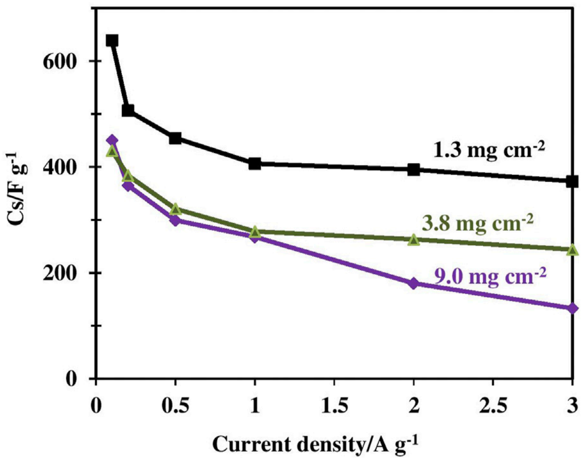

FIGURE 6
Specific capacitance obtained from the galvanostatic discharge profile at current densities ranging from 0.1 A g^{-1}–3.0 A g^{-1} with electrodes of 0.25hM_100 TiO_2 having different mass loadings.

Regarding capacity, Table 1 shows that at low current densities the higher values are exhibited by the noncrystalline material with the smaller particle size, with values reaching 704 C g^{-1}. This result indicates that surface processes such as Li surface insertion in nanometric particles and double layer formation due to the large surface area, can provide high capacity. For the two materials with larger particle sizes (0.25hM_120 and 4hR_120), the faradic reaction contributions are far from negligible, and capacities as high as 644 C g^{-1} can be obtained.

However, the nature of the process will have an important impact on the rate capability of the materials. Such an aspect is crucial for any material intended to be used in a high-power device such as a supercapacitor. Figure 5D shows the performances obtained for the four different materials as a function of the current density. The values are expressed in terms of capacitance and calculated in farads per gram considering the almost capacitive behavior of the materials. The figure indicates that the best rate capabilities are obtained for the materials dried at 100°C, which present larger surface areas, smaller particle sizes and a less crystalline nature. In particular, the amorphous 0.25hM_100 material, having a fully capacitive behavior, presents higher capacitance values, with remarkable capacitance retention at high charge density, with values of up to 400 F g^{-1} at 3 Ag^{-1}. The anatase material with the smaller particle size, i.e., 3.7 nm (4hR_100), having an almost

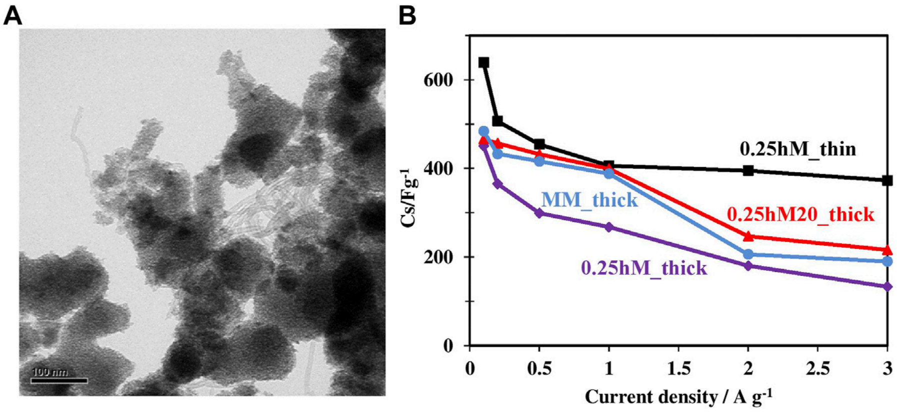

FIGURE 7
(A) TEM image of the 0.25hM10 TiO_2/CNT composite. **(B)** Comparison of the rate capabilities of electrodes based on 0.25hM TiO_2 and 20 wt% carbon black (0.2hM), its composites with 10 wt% or 20 wt% CNTs (0.25hM10 and 0.25hM20) and a mechanical mixture of TiO_2 and 20 wt% CNTs (MM). The label "thin" after the sample name indicates an electrode mass loading of approximately 1.5 mg cm^{-2} since "thick" refers to electrodes with a mass loading of approximately 9.0 mg cm^{-2}.

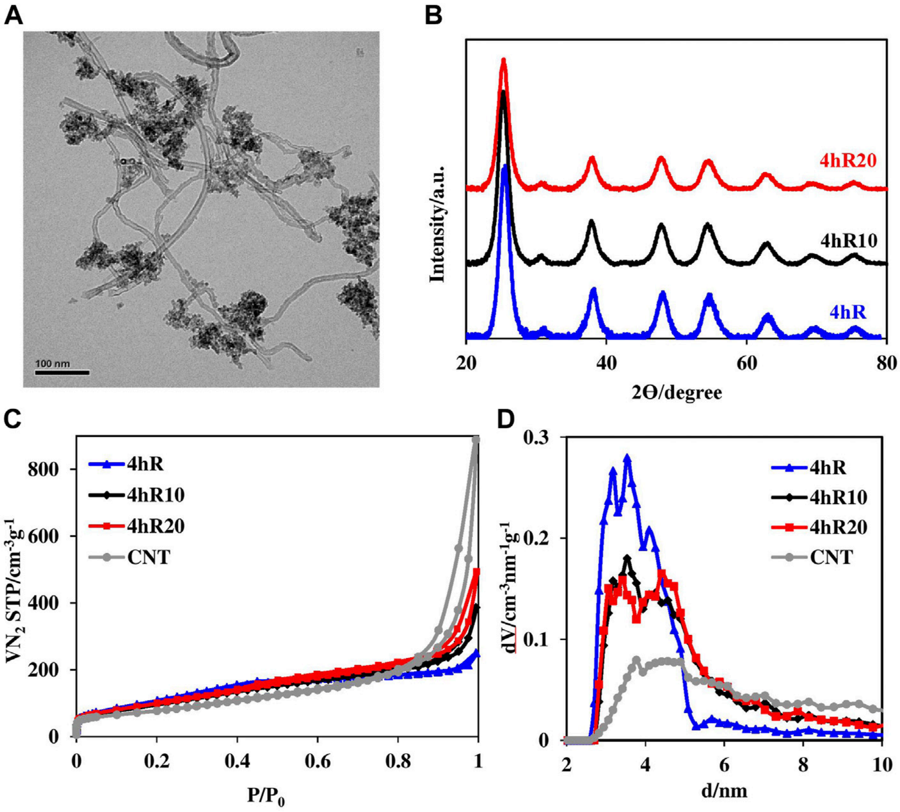

FIGURE 8
(A) TEM image of the 4hR20 TiO_2/CNT composite. Physicochemical characterization of 4hR TiO_2 and its composites with 10 wt% and 20 wt% CNTs (4hR10 and 4hR20): **(B)** XRD patterns, **(C)** N_2 adsorption isotherms and **(D)** DFT pore size distribution.

TABLE 2 Particle size and specific surface area of TiO_2 and TiO_2/CNT composites.

Sample	Particle size nm	Surface area m^2/g
0.25hM	2.0[a]	486
0.25hM20	2.0[a]	372
4hR	3.7	400
4hR10	4.0	360
4hR20	3.7	369
4hSR	5.0	378
4hSR20	5.0	384
CNT	—	265

[a]Estimated from TEM.

negligible plateau for faradic reactions, presents smaller capacitance values, but the capacitance retention at high energy density is also remarkable. However, the anatase materials with a higher contribution of faradic reactions, due to the larger particle size and smaller specific surface area, present higher capacitance values at low current densities than 4hR_100, but the decrease in the capacitance with the current density is more pronounced.

Therefore, the combination of a large surface area, nanoscale solid phase, short diffusion paths and interconnected porosity ensures that most of the active material contributes to charge storage by a pseudocapacitive mechanism. In addition, the morphology enables great discharge rates to be realized for a metal oxide.

However, due to the low conductivity of TiO_2, there is a limitation regarding the thickness of the electrodes. The above results have been obtained for thin electrodes with mass loadings of 1.2–1.4 mg cm^{-2} containing 20 wt% carbon black as a conductive additive. Figure 6 shows that increasing the mass loading of the electrodes from 1.3 mg cm^{-2} to the most reliable value, comparable to that of commercial EDLCs, of 9 mg cm^{-2} strongly degraded the capacitance and the rate capability. Such results indicate that the nanotexturation of TiO_2 into small particles decreases the Li ion paths but does not solve the conductivity drawback of TiO_2. The physical mixture of TiO_2 with a conductive additive such as carbon black is not enough for acceptable behavior at a high current density for use as an electrode in a power device such as a supercapacitor.

Therefore, to circumvent such a problem, TiO_2 has been further nanotexturated over carbon nanotubes (CNTs).

TiO_2/CNT composites

Multiwalled carbon nanotubes (CNTs) have been chosen as nanotexturing agents because of their morphology and high conductivity. It has already been proven that their high aspect ratio and extended graphitic layers allow better percolation of the active particles in an electrode than materials with other carbon-based particles such as carbon black (Raymundo-Piñero et al., 2005; Raymundo-Piñero et al., 2011; Zhu et al., 2020; Kazari et al., 2022; Keshari and Dubey, 2022).

Considering the results presented in the previous section, a composite was prepared by simply stirring the TBT–solvent mixture in the presence of CNTs. However, a morphology consisting of independent CNT networks and TiO_2 agglomerates is obtained, as presented in the TEM image in Figure 7A. The picture reveals that TiO_2 amorphous nanoparticles are densely self-assembled to form aggregates with the branched morphology previously observed for the same synthesis pathway (see TEM in Figure 3A), while CNTs agglomerate in an independent entangled network. The capacitances obtained as a function of the current density with the TiO_2/CNT composite in comparison to those obtained with the electrodes made by a physical mixture of TiO_2 with carbon black as a percolating agent (already presented in the previous section as the 0.25hM_100 material) are depicted in Figure 7B. Figure 7B shows that for a similar amount of conductive carbon, the CNTs introduced during TiO_2 synthesis allow high-mass loading electrodes to have performance similar to that of the thin electrodes with carbon black at current densities less than 1 A g^{-1}. However, for current densities higher than 1 A g^{-1}, the capacitances obtained with the TiO_2/CNT composites, even if they are higher than those of an 0.25hM electrode with carbon black loaded with the same mass, do not attain the values obtained with the thin electrodes. In fact, Figure 7B shows that the TiO_2/CNT composite possesses the same rate capability as a physical mixture on TiO_2 with the same amount of CNTs (sample MM). These results confirm that simple stirring of the TBT–solvent mixture in the presence of CNTs leads to independent TiO_2 and CNT networks. Although the results presented in Figure 7B show that CNTs are better percolating agents than carbon black, this kind of physical mixture of TiO_2 and CNTs does not allow thick electrodes with high capacitances to be obtained at high current density.

Therefore, to favor the interaction between the CNTs and the TiO_2 precursor during sol–gel synthesis, the strategy was to perform solution reflux as presented above. Figure 8A shows that after 4 h of reflux, the TiO_2 nanoparticles grew over the CNTs, forming small aggregates over their surface. Figure 8B shows that a crystalline TiO_2 anatase phase formed as the majority phase regardless of the amount of CNTs used. Brookite is found as a minority phase, with a percentage less than 1%. The size of TiO_2 nanoparticles, determined as described in the experimental section, is in the range of 3–4 nm regardless of the %w CNTs. The nanoparticle diameter is included in Table 2. These results indicate that adding CNTs to the synthesis medium does not influence the particle size or crystallinity. The position of the main peaks changes, revealing a chemical interaction between the CNTs and TiO_2 nanoparticles. Therefore, some TiO_2 nanoparticles anchor to the

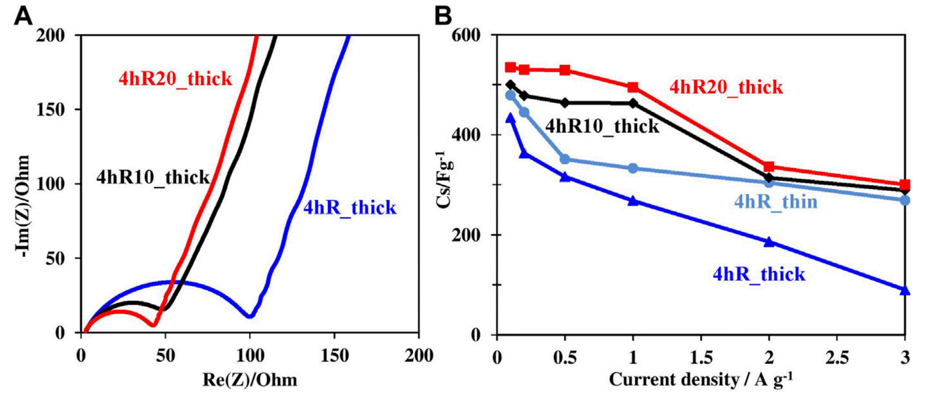

FIGURE 9
Electrochemical characterization of the electrodes based on 4hR TiO_2 with 20 wt% carbon black (4hR) and its composites with 10 wt% and 20 wt% CNTs (4hR10 and 4hR20) in $LiPF_6$ EC/PC/3DMC as the electrolyte: **(A)** Nyquist plot and **(B)** rate capability. The label "thin" after the sample name indicates an electrode mass loading of approximately 1.5 mg cm^{-2} since "thick" refers to electrodes with a mass loading of approximately 9.0 mg cm^{-2}.

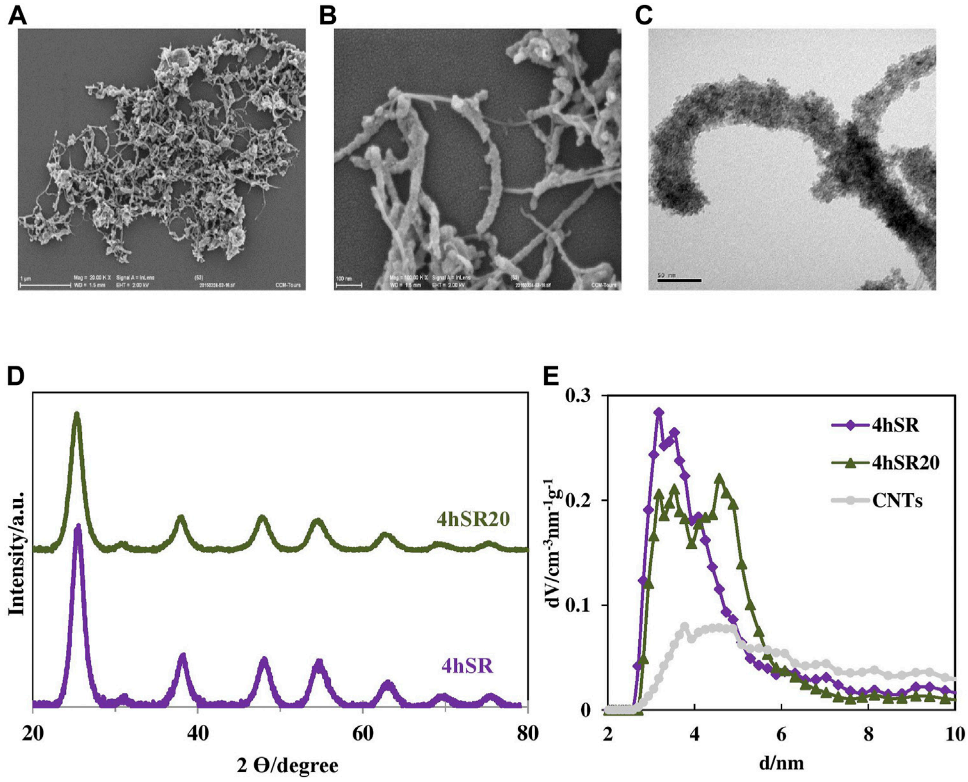

FIGURE 10
(A) SEM image, **(B)** HR SEM image and **(C)** TEM image of the 4hsR20 TiO_2/CNT composite. Physicochemical characterization of 4hSR TiO_2 and its composite with 20 wt% CNTs (4hSR20): **(D)** XRD patterns and **(E)** DFT pore size distribution.

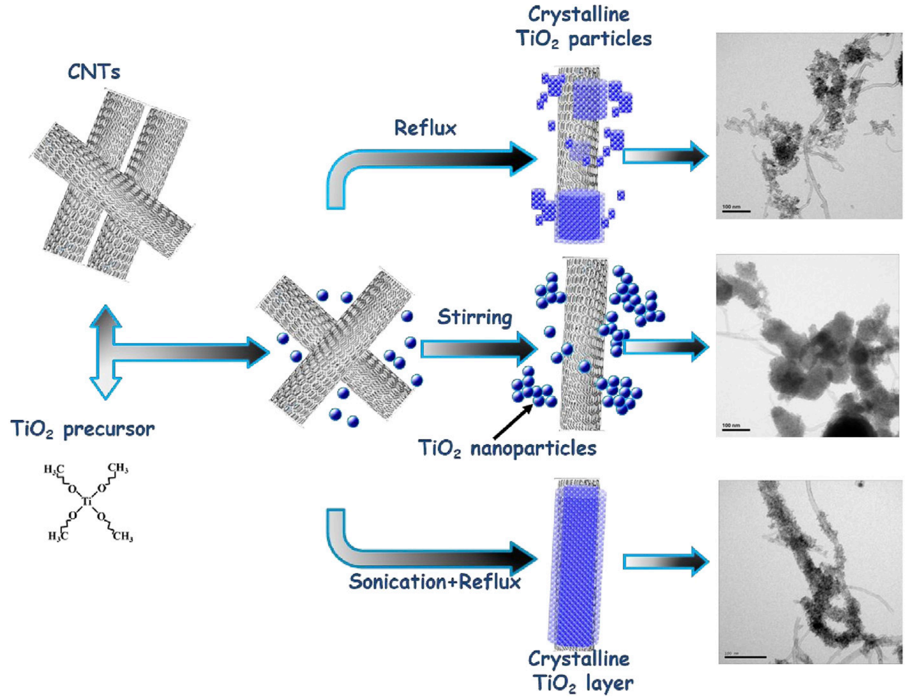

FIGURE 11
Schema of the different TiO_2/CNT composite synthesis pathways and a TEM image of the resulting composite.

CNT surface. Figure 8C shows the effect of adding 10 wt% or 20 wt% CNTs on the porous texture of the materials (materials 4hR10 and 4hR20, respectively). The N_2 adsorption isotherm of CNTs is typical of a mesoporous material. The mesopores are mainly formed by the entanglement of the nanotubes, as they are essentially closed. By the addition of CNTs to TiO_2 during the synthesis step, N_2 adsorption is almost unmodified in the relative pressure region smaller than 0.6, whereas a noticeable enhancement at $P/P_0 > 0.6$ in the range of CNT mesoporosity is observed. Therefore, the specific surface area is almost not modified by the presence of CNTs, whereas the pore size distribution (Figure 8D) reveals the presence of mesopores in the diameter range for the CNTs in the composites. The amount of mesopores in such a range increases with the amount of CNTs in the composite. The quantitative data extracted from the N_2 adsorption isotherms are given in Table 2.

Figure 9 shows that such TiO_2 nanotexturation on small aggregates over the CNT network increases the conductivity of high-mass loading electrodes in the organic electrolyte. The Nyquist plots presented in the Figure 9A confirm a noticeable decrease in the resistance for the composites prepared with CNTs (4hR10 and 4hR20) in comparison to a standard electrode prepared with carbon black (4hR). Increasing the amount of CNTs from 10 wt% to 20 wt% leads to a small decrease in the resistance. The effect of CNTs on the resistance decrease is attributed, on the one hand, to the fact that this kind of network of conducting CNTs is able to efficiently connect the particles of TiO_2 in the composites (see the TEM image in Figure 8A). On the other hand, is the CNTs have a nanotexturing effect on the composite, which appears as a network of open mesopores (Figures 8C,D) facilitating the diffusion of ions to the small aggregates of TiO_2 particles. Therefore, CNTs allow for high-mass loading electrodes with a percolated network. Figure 9B shows that this feature has a remarkable impact on the rate capability of such high-mass loading electrodes. The addition of 10 wt% CNTs to the composite significantly enhances the specific capacitance at high current densities, and an increase in the CNT fraction to 20 wt% provokes a further improvement in the performance. For low current densities, the TiO_2/CNT composites clearly outperform the TiO_2 electrodes with carbon black having the same mass loading and even the thin electrodes. For high current densities, the TiO_2/CNT composites behave similarly to the thin electrodes. Hence, the TiO_2 nanotexturation in small aggregates intimately connected to the open CNT network allows high-mass loading electrodes to operate with an enhanced rate capability.

As a strong TiO_2–CNT interaction is at the core of the remarkable electrochemical performance shown in Figure 9B, the synthesis pathway was further modified to improve this interaction. The SEM image presented in Figure 10A illustrates that sonicating the TBT–solvent mixture in the presence of CNTs before solution reflux leads to an entangled

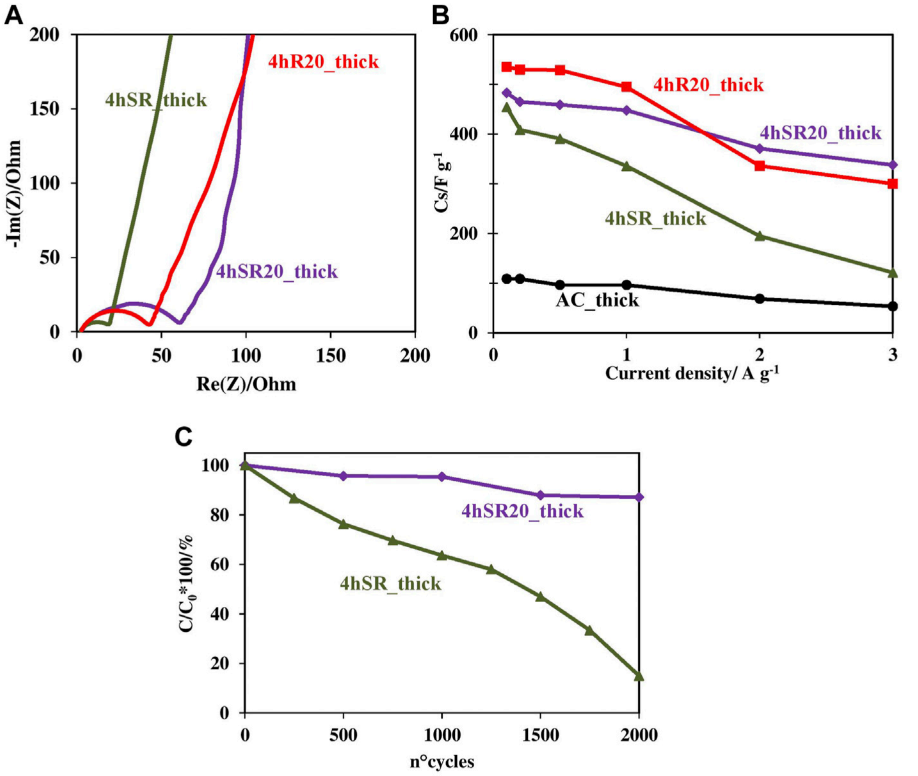

FIGURE 12
Electrochemical characterization of the electrodes based on 4hSR TiO_2 with 20 wt% carbon black (4hSR) and its composite with 20 wt% CNTs (4hSR20) in $LiPF_6$ EC/PC/3DMC as the electrolyte: **(A)** Nyquist plot compared to the composite 4hR20, **(B)** rate capability compared to the composite 4hR20 and commercial activated carbon (AC) and **(C)** cycle performance at a current density of 0.5 A g^{-1}. The label "thick" after the sample name indicates an electrode mass loading of approximately 9.0 mg cm^{-2}.

network of nanotube-like morphologies. The FE-SEM image in Figure 10B reveals that the nanotubes are carbon nanotubes covered by TiO_2 nanoparticles. The TEM image in Figure 10C confirms the presence of a homogeneous coating of TiO_2 nanoparticles on the surface of the CNTs. Besides the effect that it can have on the CNTs dispersion, sonication drives to the formation of surface defects and oxygenated functionalities in the CNTs surface improving the interfacial interactions by acting as actives sites for chemical reaction during TiO_2 nucleation (Rossel et al., 2013; Maleki, 2018).

Although the morphology of the composites is very different than that obtained just by reflux, the additional sonication step does not influence the TiO_2 crystallinity or particle size, as shown by the XRD pattern in Figure 10D and Table 2. TiO_2 nanoparticles are well crystallized as anatase, and the particle size is 5 nm, corresponding to the particle size found for the same synthesis pathway in the absence of CNTs (see sample 4hSR in Figure 10D and Table 2). Nevertheless, the small shift in the XRD peaks again reveals the strong chemical interaction between the TiO_2 nanoparticles and the CNTs. The pore size distribution obtained from N_2 adsorption (see Figure 10E) is additional evidence of the nanotexturation of the TiO_2 particles with an open mesoporous network in the diameter size range of the CNTs.

Therefore, the presence of CNTs during sol–gel synthesis does not influence the TiO_2 particle size and crystallinity. However, as shown in Figure 11, the way the CNTs and the TiO_2 precursor solution were mixed has a nonnegligible impact on the TiO_2 and CNT interaction leading to different morphologies of the composites. The morphology has an important effect on the electrochemical behavior of the composite.

In particular, the uniform coverage of small TiO_2 particles on the surface of the entangled and well interconnected CNT network obtained by using sonication and reflux increases the conductivity and improves the access of the electrolyte to the active material. In this sense, the Nyquist plot presented in Figure 12A displays the decrease in the resistance when nanotexturing TiO_2 over carbon nanotubes (sample 4hSR20 with 20 wt% CNTs) in comparison with the same material prepared in the absence of CNTs but having the same amount of carbon black (sample 4hSR with 20 wt%

carbon black). Moreover, the resistance is reduced in comparison with that of the TiO_2/CNT composite prepared only by reflux (4hR20). As a consequence, Figure 12B shows that the rate capability follows the same trend as the resistance. For high-mass loading electrodes, the use of CNTs clearly improves the rate capability. Moreover, the figure reveals that nanotexturation of TiO_2 as a homogeneous layer over the CNTs (4hSR20 material) instead of small aggregates intimately connected to the open CNT network (4hR20 material) allowed higher capacitances to be obtained at high current densities and therefore increased the power capability. In particular, the presence of CNTs allows keeping 70% of the capacitance at high current densities while only 27% is retained when using a regular conductivity agent as carbon black. It is worth to remark that our TiO_2 composites demonstrated a better rate capability than in various reports about the performance of TiO_2 in Li based organic electrolytes using lower mass electrodes. For instance, TiO_2-Polipyrrol-single walled nanotubes electrodes with 0.7 mg cm^{-2} yielded 22% capacitance retention at 2 A g^{-1} (Tang et al., 2017) and TiO_2 nanoparticles showed 52% at 3 A g^{-1} (Shin et al., 2011). Also, thick electrodes with our TiO_2/CNTs composites showed much better capacitance retention than other TiO_2-carbon composites with maximum values of 51% at 3 A g^{-1} (Lee et al., 2019). Figure 12B also shows that the capacitances obtained in all the ranges of current densities clearly outperform those obtained for a commercial porous carbon usually used for EDLCs (AC material).

Another advantage of using CNTs as nanotexturing agents is an improvement in the cycle life (Figure 12C). Actually, the nanotubes prevent the loss of electrode integrity during cycling by accommodating the possible dimensional changes of the TiO_2 nanoparticles during Li ion insertion/disinsertion even when there is a high mass loading in the electrodes.

In summary, the nanotexturation of TiO_2 in nanoparticles homogeneously deposited over CNTs forming an entangled and interconnected open mesoporous network allows a decrease in the Li ion paths and the accessibility of ions to the active mass, and consequently, charge propagation is improved. Such nanotexturation allows thick electrodes operating in organic electrolytes to have a high capacitance and the rate capability desired for developing supercapacitors with high energy density and high power density.

Conclusion

A synthesis protocol based on a green sol-gel method without using any surfactants or unsafe additives was developed to obtain TiO_2 with a small particle size and large specific surface area (2–5 nm and up to 460 m^2 g^{-1}, respectively). The electrochemical signature in an organic electrolyte of an intrinsically faradic oxide is now fully capacitive, indicating fast pseudofaradic Li intercalation reactions at the electrode/electrolyte interface, even if the galvanostatic charge/discharge step is performed at a very low charge density (0.1 A g^{-1}). Capacitances as high as 600 F g^{-1} can be extracted, outperforming standard porous carbon behavior in the same electrolyte. However, because of the low electronic conductivity of TiO_2, even if 20 wt% carbon black is mixed with TiO_2, only very thin electrodes with a low active material loading are able to deliver high specific capacitances at high current densities. In such a case, implementation in real devices is not reliable. Therefore, the nanotexturation of TiO_2 over a percolating agent with a highly interconnected network such as CNTs has been shown to be a solution to the lack of conductivity at the same time that the access of the electrolyte to the active electrode material is enhanced. Such uniform nanotexturation of TiO_2 allows good rate capabilities to be obtained for thick electrodes having enough active material loading to obtain high specific energy and power densities. Hence, TiO_2/CNT composites can overcome one of the most serious bottlenecks when developing metal compounds as electrodes for pseudocapacitors, which is the negative impact of mass loading on the delivered rate capability.

Data availability statement

The original contributions presented in the study are included in the article/Supplementary Material, further inquiries can be directed to the corresponding author.

Author contributions

ER-P and NP contributed to the conception and design of the study and to the acquisition of funding support. The experiments were conducted by NP, VR, RO, and RM. ER-P and NP analyzed and organized the results. The manuscript was drafted by ER-P and NP contributed to editing the manuscript. All authors contributed to manuscript revision and read and approved of the submitted version.

Acknowledgments

The authors thank the Région Centre val de Loire (Projects APR-IR SCAP-3D, convention n°2017-00117284, and Superherox, convention n°2013 00083164) for financial support.

Conflict of interest

The authors declare that the research was conducted in the absence of any commercial or financial relationships that could be construed as a potential conflict of interest.

Publisher's note

References

Augustyn, V., Simon, P., and Dunn, B. (2014). Pseudocapacitive oxide materials for high-rate electrochemical energy storage. *Energy Environ. Sci.* 7, 1597. doi:10.1039/C3EE44164D

Barzegar, F., Bello, A., Momodu, D. Y., Dangbegnon, J. K., Taghizadeh, F., Madito, M. J., et al. (2015). Asymmetric supercapacitor based on an α-MoO$_3$ cathode and porous activated carbon anode materials. *RSC Adv.* 5, 37462–37468. doi:10.1039/c5ra03579a

Brandt, A., and Balducci, A. (2014). Theoretical and practical energy limitations of organic and ionic liquid-based electrolytes for high voltage electrochemical double layer capacitors. *J. Power Sources* 250, 343–351. doi:10.1016/j.jpowsour.2013.10.147

Brezesinski, T., Wang, J., Polleux, J., Dunn, B., and Tolbert, S. H. (2009). Templated nanocrystal-based porous TiO2 films for next-generation electrochemical capacitors. *J. Am. Chem. Soc.* 131, 1802–1809. doi:10.1021/ja8057309

Brousse, T., Bélanger, D., and Long, J-W. (2015). Be or not to Be pseudocapacitive? *J. Electrochem. Soc.* 162 (5), A5185–A5189. doi:10.1149/2.0201505jes

Cargnello, M., Gordon, T. R., and Murray, C. B. (2014). Solution-phase synthesis of titanium dioxide nanoparticles and nanocrystals. *Chem. Rev.* 114, 9319–9345. doi:10.1021/cr500170p

Chen, D., Huang, F., Cheng, Y-B., and Caruso, R. A. (2009). Mesoporous anatase TiO$_2$ beads with high surface areas and controllable pore sizes: A superior candidate for high-performance dye-sensitized solar cells. *Adv. Mat.* 21, 2206–2210. doi:10.1002/adma.200802603

Chen, H. S., and Kumar, R. V. (2012). Sol–gel TiO2 in self-organization process: Growth, ripening and sintering. *RSC Adv.* 2, 2294. doi:10.1039/c2ra00782g

Chen, K., Noh, Y. D., Huang, W., Ma, J., Komarneni, S., and Xue, D. (2014). Microwave-hydrothermal synthesis of Fe-based materials for lithium-ion batteries and supercapacitors. *Ceram. Int.* 40, 2877–2884. doi:10.1016/j.ceramint.2013.10.024

Chen, S., Zhu, J., Wu, X., Han, Q., and Wang, X. (2010). Graphene oxide MnO$_2$ nanocomposites for supercapacitors. *ACS Nano* 4, 2822–2830. doi:10.1021/nn901311t

Chen, X., and Mao, S. (2007). Titanium dioxide Nanomaterials: synthesis, properties, modifications, and applications. *Chem. Rev.* 107, 2891–2959. doi:10.1021/cr0500535

Choudhary, N., Li, C., Moore, J., Nagaiah, N., Lei Zhai, L., Jung, Y., et al. (2017). Asymmetric supercapacitor electrodes and devices. *Adv. Mat.* 29, 1605336. doi:10.1002/adma.201605336

Courtin, E., Boy, P., Piquero, T., Vulliet, J., Poirot, N., and Laberty-Robert, C. (2012). A composite sol–gel process to prepare a YSZ electrolyte for Solid Oxide Fuel Cells. *J. Power Sources* 206, 77–83. doi:10.1016/j.jpowsour.2012.01.109

Cushing, B. L., Kolesnichenko, V. L., and O'Connor, C. J. (2004). Recent advances in the liquid-phase syntheses of inorganic nanoparticles. *Chem. Rev.* 104, 3893–3946. doi:10.1021/cr030027b

Debecker, D. P., and Mutin, P. H. (2012). Non-hydrolytic sol–gel routes to heterogeneous catalysts. *Chem. Soc. Rev.* 41, 3624. doi:10.1039/c2cs15330k

Devaraj, S., and Munichandraiah, N. (2008). Effect of crystallographic structure of MnO$_2$ on its electrochemical capacitance properties. *J. Phys. Chem. C* 112, 4406–4417. doi:10.1021/jp7108785

Gao, J., Qiu, G., Li, H., Li, M., Li, C., Qian, L., et al. (2020). Boron-doped graphene/TiO2 nanotube-based aqueous lithium ion capacitors with high energy density. *Electrochimica Acta* 329, 135175. doi:10.1016/j.electacta.2019.135175

Gao, Z-H., Zhang, H., Cao, G-P., Han, M-F., and Yang, Y-S. (2013). Spherical porous VN and NiOx as electrode materials for asymmetric supercapacitor as electrode materials for asymmetric supercapacitor. *Electrochimica Acta* 87, 375–380. doi:10.1016/j.electacta.2012.09.075

Ge, M., Cao, C., Huang, J., Li, S., Chen, Z., Zhang, K-Q., et al. (2016). A review of one-dimensional TiO$_2$ nanostructured materials for environmental and energy applications. *J. Mat. Chem. A Mat.* 4, 6772–6801. doi:10.1039/c5ta09323f

Ghodbane, O., Pascal, J. L., and Favier, F. (2009). Microstructural effects on charge-storage properties in MnO$_2$-based electrochemical supercapacitors. *ACS Appl. Mat. Interfaces* 1, 1130–1139. doi:10.1021/am900094e

Hu, Z. A., Xie, Y. L., Wang, Y. X., Xie, L. J., Fu, G. R., Jin, X. Q., et al. (2009). Synthesis of α-cobalt hydroxides with different intercalated anions and effects of intercalated anions on their morphology, basal plane spacing, and capacitive property. *J. Phys. Chem. C* 113, 12502–12508. doi:10.1021/jp8106809

Huang, M., Li, F., Dong, F., Zhang, Y-X., and Zhang, L. (2015). MnO$_2$-based nanostructures for high-performance supercapacitors. *J. Mat. Chem. A Mat.* 3, 21380–21423. doi:10.1039/c5ta05523g

Jiang, C., Wei, M., Qi, Z., Kudo, T., Honma, I., and Zhou, H. (2007). Particle size dependence of the lithium storage capability and high rate performance of nanocrystalline anatase TiO2 electrode. *J. Power Sources* 166, 239–243. doi:10.1016/j.jpowsour.2007.01.004

Jiao, F., and Bruce, P. G. (2007). Mesoporous crystalline α-MnO$_2$—A reversible positive electrode for rechargeable lithium batteries. *Adv. Mat.* 19, 657–660. doi:10.1002/adma.200602499

Kazari, H., Pajootan, E., Hubert, P., and Coulombe, S. (2022). Dry synthesis of binder-free ruthenium nitride-coated carbon nanotubes as a flexible supercapacitor electrode. *ACS Appl. Mat. Interfaces* 14 (13), 15112–15121. doi:10.1021/acsami.1c22276

Keshari, A. S., and Dubey, P. (2022). Amorphous MnO$_x$ nanostructure/multiwalled carbon nanotube composites as electrode materials for supercapacitor applications. *ACS Appl. Nano Mat.* 5 (6), 8566–8582. doi:10.1021/acsanm.2c02040

Lee, Y., Kim, S., Lee, J. H., Roh, K. C., Lim, E., and Lee, J. (2019). Improved pseudocapacitive charge storage in highly ordered mesoporous TiO$_2$/carbon nanocomposites as high-performance Li-ion hybrid supercapacitor anodes. *RSC Adv.* 9, 37882–37888. doi:10.1039/c9ra07157a

Li, W., Wang, F., Feng, S., Wang, J., Sun, Z., Li, B., et al. (2013). Sol–Gel design strategy for ultradispersed TiO$_2$ nanoparticles on graphene for high-performance lithium ion batteries. *J. Am. Chem. Soc.* 135, 18300–18303. doi:10.1021/ja4100723

Liu, T., Zhang, L., You, W., and Yu, J. (2018). Core–shell nitrogen-doped carbon hollow spheres/Co$_3$O$_4$ nanosheets as advanced electrode for high-performance supercapacitor. *Small* 14, 1702407. doi:10.1002/smll.201702407

Lokhande, V., Lokhande, A., Namkoong, G., Kim, J. H., and Ji, T. (2019). Charge storage in WO$_3$ polymorphs and their application as supercapacitor electrode material. *Results Phys.* 12, 2012–2020. doi:10.1016/j.rinp.2019.02.012

Lu, X., Lu, M., Wang, G., Zhai, T., Xie, S., Ling, Y., et al. (2013). H-TiO2@MnO 2//H-TiO 2@C core–shell nanowires for high performance and flexible asymmetric supercapacitors. *Adv. Mat.* 25, 267–272. doi:10.1002/adma.201203410

Maleki, A. (2018). Green oxidation protocol: Selective conversions of alcohols and alkenes to aldehydes, ketones and epoxides by using a new multiwall carbon nanotubebased hybrid nanocatalyst via ultrasound irradiation. *Ultrason. Sonochem.* 40, 460–464. doi:10.1016/j.ultsonch.2017.07.020

Mor, G. K., Varghese, O. K., Paulose, M., and Grimes, C. A. (2005). Transparent highly ordered TiO$_2$ nanotube Arrays via anodization of titanium thin films. *Adv. Funct. Mat.* 15, 1291–1296. doi:10.1002/adfm.200500096

Niederberger, M., Bartl, M. H., and Stucky, G. D. (2002). Benzyl alcohol and transition metal chlorides as a versatile reaction system for the nonaqueous and low-temperature synthesis of crystalline nano-objects with controlled dimensionality. *J. Am. Chem. Soc.* 14, 13642–13643. doi:10.1021/ja027115i

Niederberger, M., and Garnweitner, G. (2006). Organic reaction pathways in the nonaqueous synthesis ofMet al Oxidenanoparticles. *Chem. Eur. J.* 12, 7282–7302. doi:10.1002/chem.200600313

Niederberger, M. (2007). Nonaqueous sol–gel routes to metal oxide nanoparticles. *Acc. Chem. Res.* 40, 793–800. doi:10.1021/ar600035e

Poirot, N., Bregiroux, D., Boy, P., Autret-Lambert, C., Belleville, P., and Bianchi, L. (2015). Sintering of nanostructured Sc$_2$O$_3$ ceramics from sol–gel-derived nanoparticles. *Ceram. Int.* 41, 3879–3887. doi:10.1016/j.ceramint.2014.11.067

Ramandoss, A., and Kim, S. J. (2013). Vertically aligned TiO2 nanorod arrays for electrochemical supercapacitor. *J. Alloys Compd.* 561, 262–267. doi:10.1016/j.jallcom.2013.02.015

Raymundo-Piñero, E., Cadek, M., Wachtler, M., and Beguin, F. (2011). Carbon nanotubes as nanotexturing agents for high power supercapacitors based on seaweed carbons. *ChemSusChem* 4, 943–949. doi:10.1002/cssc.201000376

Raymundo-Piñero, E., Khomenko, V., Frackowiak, E., and Béguin, F. (2005). Performance of manganese oxide/CNTs composites as electrode materials for electrochemical capacitors. *J. Electrochem. Soc.* 152, A229. doi:10.1149/1.1834913

Razaa, W., Alib, F., Razac, N., Luoa, Y., Kim, K-H., Yanga, J., et al. (2018). Recent advancements in supercapacitor technology. *Nano Energy* 52, 441–473. doi:10.1016/j.nanoen.2018.08.013

Rossel, M. D., Kuebel, C., Ilari, G., Rechberger, F., Heiligtag, F. J., Niederberger, M., et al. (2013). Impact of sonication pretreatment on carbon nanotubes: A transmission electron microscopy study. *Carbon* 61, 404–411. doi:10.1016/j.carbon.2013.05.024

Salari, M., Konstantinov, K., and Liu, H. K. (2011). Enhancement of the capacitance in TiO2 nanotubes through controlled introduction of oxygen vacancies. *J. Mat. Chem.* 21, 5128. doi:10.1039/C0JM04085A

Shao, Z., Li, H., Li, M., Li, C., Qu, C., and Yang, B. (2015). Fabrication of polyaniline nanowire/TiO_2 nanotube array electrode for supercapacitors. *Energy* 87, 578–585. doi:10.1016/j.energy.2015.05.025

Shin, J.-Y., Samuelis, D., and Maier, J. (2011). Sustained lithium-storage performance of hierarchical, nanoporous anatase TiO_2 at high rates: Emphasis on interfacial storage phenomena. *Adv. Funct. Mat.* 21, 3464–3472. doi:10.1002/adfm.201002527

Subramanian, V., Karki, A., Gnanasekar, K. I., Eddy, F. P., and Rambabu, B. (2006). Nanocrystalline TiO_2(anatase) for Li-ion batteries. *J. Power Sources* 159, 186–192. doi:10.1016/j.jpowsour.2006.04.027

Sudant, G., Baudrin, E., Larcher, D., and Tarascon, J. M. (2005). Electrochemical lithium reactivity with nanotextured anatase-type TiO2. *J. Mat. Chem.* 15, 1263. doi:10.1039/b416176a

Szeifert, J. M., Feckl, J. M., Fattakhova-Rohlfing, D., Liu, Y., Kalousek, V., Rathousky, J., et al. (2010). Ultrasmall titania nanocrystals and their direct assembly into mesoporous structures showing fast lithium insertion. *J. Am. Chem. Soc.* 132, 12605–12611. doi:10.1021/ja101810e

Tang, G., Gao, L., Xiao, P., Zhang, Y., and Liu, H. (2017). A novel high energy hybrid Li-ion capacitor with a three-dimensional hierarchical ternary nanostructure of hydrogen-treated TiO_2 nanoparticles/conductive polymer/carbon nanotubes anode and an activated carbon cathode. *J. Power Sources* 355, 1–7. doi:10.1016/j.jpowsour.2017.04.053

Wang, F., Wang, C., Zhao, Y., Liu, Z., Chang, Z., Fu, L., et al. (2016). A quasi-solid-state Li-ion capacitor based on porous TiO_2 hollow microspheres wrapped with graphene nanosheets. *small* 12 (45), 6207–6213. doi:10.1002/smll.201602331

Wang, J., Polleux, J., Lim, J., and Dunn, B. (2007). Pseudocapacitive contributions to electrochemical energy storage in TiO2 (anatase) nanoparticles. *J. Phys. Chem. C* 111, 14925–14931. doi:10.1021/jp074464w

Wang, Q., Wen, Z., and Li, J. (2006). A hybrid supercapacitor fabricated with a carbon nanotube cathode and a TiO_2–B nanowire anode. *Adv. Funct. Mat.* 16, 2141–2146. doi:10.1002/adfm.200500937

Wang, Z., and Lou, X. W. (2012). TiO_2 nanocages: Fast synthesis, interior functionalization, and improved lithium storage properties. *Adv. Mat.* 24, 4124–4129. doi:10.1002/adma.201104546

Xu, H., Hu, X., Yang, H., Sun, Y., Hu, C., and Huang, Y. (2015). Flexible asymmetric micro-supercapacitors based on Bi2O3 and MnO_2 nanoflowers: Larger areal mass promises higher energy density. *Adv. Energy Mat.* 5, 1401882. doi:10.1002/aenm.201401882

Xu, W., Dai, S., Liu, G., Xi, Y., Hu, C., and Wang, X. (2016). CuO nanoflowers growing on carbon fiber fabric for flexible high-performance supercapacitors. *Electrochimica Acta* 203, 1–8. doi:10.1016/j.electacta.2016.03.170

Yu, L., Hu, H., Wu, H. B., and Lou, X. W. (2017). Complex hollow nanostructures: Synthesis and energy-related applications. *Adv. Mat.* 29, 1604563. doi:10.1002/adma.201604563

Zhang, H., and Banfield, J. F. (2000). Understanding polymorphic phase transformation behavior during growth of nanocrystalline aggregates: Insights from TiO2. *J. Phys. Chem. B* 104, 3481–3487. doi:10.1021/jp000499j

Zhang, Y., Zheng, J., Zhao, Y., Hu, T., Gao, Z., and Meng, C. (2016). Fabrication of V_2O_5 with various morphologies for high-performance electrochemical capacitor. *Appl. Surf. Sci.* 377, 385–393. doi:10.1016/j.apsusc.2016.03.180

Zhao, D. D., Bao, S. J., Zhou, W. J., and Li, H. L. (2007). Preparation of hexagonal nanoporous nickel hydroxide film and its application for electrochemical capacitor. *Electrochem. Commun.* 9, 869–874. doi:10.1016/j.elecom.2006.11.030

Zheng, J. P., and Jow, T. R. (1995). A new charge storage mechanism for electrochemical capacitors. *J. Electrochem. Soc.* 142, L6–L8. doi:10.1149/1.2043984

Zhou, H., and Zhang, Y. (2014). Electrochemically self-doped TiO_2 nanotube Arrays for supercapacitors. *J. Phys. Chem. C* 118, 5626–5636. doi:10.1021/jp4082883

Zhu, S., Ni, J., and Li, Y. (2020). Carbon nanotube-based electrodes for flexible supercapacitors. *Nano Res.* 13, 1825–1841. doi:10.1007/s12274-020-2729-5